Draft version July 16, 2012
Preprint typeset using LaTeX style emulateapj v. 5/2/11

HAT-P-39b–HAT-P-41b: THREE HIGHLY INFLATED TRANSITING HOT JUPITERS †

J. D. Hartman[1], G. Á. Bakos[1,2], B. Béky[3], G. Torres[3], D. W. Latham[3], Z. Csubry[1], K. Penev[1], A. Shporer[4,5], B. J. Fulton[4], L. A. Buchhave[6], J. A. Johnson[7], A. W. Howard[8], G. W. Marcy[8], D. A. Fischer[9], G. Kovács[10,11], R. W. Noyes[3], G. A. Esquerdo[3], M. Everett[3], T. Szklenár[3], S. N. Quinn[3,12], A. Bieryla[3], R. P. Knox[13], P. Hinz[13], D. D. Sasselov[3], G. Fűrész[3], R. P. Stefanik[3], J. Lázár[14], I. Papp[14], P. Sári[14],

Draft version July 16, 2012

ABSTRACT

We report the discovery of three new transiting extrasolar planets orbiting moderately bright (V = 11.1 to 12.4) F stars. The planets have periods of P = 2.6940 d to 4.4572 d, masses of 0.60 $M_{\rm J}$ to 0.80 $M_{\rm J}$, and radii of 1.57 $R_{\rm J}$ to 1.73 $R_{\rm J}$. They orbit stars with masses between 1.40 $M_{\odot}$ and 1.51 $M_{\odot}$. The three planets are members of an emerging population of highly inflated Jupiters with 0.4 $M_{\rm J} < M <$ 1.5 $M_{\rm J}$ and $R >$ 1.5 $R_{\rm J}$.

Subject headings: planetary systems — stars: individual (HAT-P-39, GSC 1364-01424, HAT-P-40, GSC 3607-01028, HAT-P-41, GSC 0488-02442) — techniques: spectroscopic, photometric

1. INTRODUCTION

Transiting exoplanets (TEPs) are key objects for the study of planets outside the Solar System. The geometry of these planetary systems enables measurements of several important physical parameters, such as planetary masses and radii, or the sky-projected angle between the orbital axis of a planet and the spin axis of its host star (e.g. Queloz et al. 2000). The vast majority of well-characterized TEPs (i.e. TEPs with measured masses and radii) have been discovered by dedicated photometric surveys, including the Wide Angle Search for Planets (WASP; Pollacco et al. 2006), the Hungarian-made Automated Telescope Network (HATNet; Bakos et al. 2004) and its southern extension (HATSouth; Bakos et al. 2012), Kepler (Borucki et al. 2010), CoRoT (Barge et al. 2008), OGLE (Udalski et al. 2002), TrES (Alonso et al. 2004), XO (McCullough et al. 2006), the Qatar Exoplanet Survey (QES; Alsubai et al. 2011), the Kilodegree Extremely Little Telescope survey (KELT; Siverd et al. 2012), and MEarth (Charbonneau et al. 2009).

Significant among these are the ground-based, wide-field surveys using small aperture telescopes, including WASP, HATNet, HATSouth, TrES, XO, QES, and KELT. While these surveys are heavily biased towards discovering large planets on short-period orbits compared to the Kepler and CoRoT space-based surveys, the planets discovered by ground-based surveys tend to orbit stars that are brighter than those discovered by the space-based surveys, making such planets more amenable to detailed characterization and follow-up studies (this is true as well for the few, but valuable, transiting planets discovered by RV searches, which are found around even brighter stars than those discovered by photometric surveys). Additionally the extreme environments in which these planets are discovered, while perhaps not representative of most planetary systems, create a natural experiment for testing theories of planet structure and formation. For example, a number of gas-giant planets have been discovered with radii that are substantially larger than theoretically expected (e.g. Mandushev et al. 2007; Collier Cameron et al. 2007; Snellen et al. 2009; Hebb et al. 2009; Latham et al. 2010; Fortney et al. 2011; Anderson et al. 2010, 2011; Enoch et al. 2011; Hartman et al. 2011; Smalley et al. 2012). These have been used to empirically determine the factors affecting the radii of planets (e.g. Enoch et al. 2012) which in turn informs theoretical work on the subject.

In this paper we present the discovery and characterization of three new transiting planets around the relatively bright stars GSC 1364-01424, GSC 3607-01028, and GSC 0488-02442, by the HATNet survey. As members of the growing sample of highly inflated planets, these objects will provide valuable leverage for under-

[1] Department of Astrophysical Sciences, Princeton University, Princeton, NJ 08544; email: gbakos@astro.princeton.edu
[2] Sloan Fellow
[3] Harvard-Smithsonian Center for Astrophysics, Cambridge, MA
[4] LCOGT, 6740 Cortona Drive, Santa Barbara, CA
[5] Department of Physics, Broida Hall, UC Santa Barbara, CA
[6] Niels Bohr Institute, University of Copenhagen, DK-2100, Denmark, and Centre for Star and Planet Formation, Natural History Museum of Denmark, DK-1350 Copenhagen
[7] California Institute of Technology, Department of Astrophysics, MC 249-17, Pasadena, CA
[8] Department of Astronomy, University of California, Berkeley, CA
[9] Astronomy Department, Yale University, New Haven, CT
[10] Konkoly Observatory, Budapest, Hungary
[11] Department of Physics and Astrophysics, University of North Dakota, Grand Forks, ND
[12] Department of Physics and Astronomy, Georgia State University, Atlanta, GA
[13] Steward Observatory, University of Arizona, Tucson, AZ
[14] Hungarian Astronomical Association, Budapest, Hungary

† Based in part on observations obtained at the W. M. Keck Observatory, which is operated by the University of California and the California Institute of Technology. Keck time has been granted by NOAO (A201Hr, A289Hr, A284Hr), NASA (N049Hr, N018Hr, N167Hr, N029Hr, N108Hr, N154Hr), and the NOAO Gemini/Keck time-exchange program (G329Hr). Based in part on observations made with the Nordic Optical Telescope, operated on the island of La Palma jointly by Denmark, Finland, Iceland, Norway, and Sweden, in the Spanish Observatorio del Roque de los Muchachos of the Instituto de Astrofisica de Canarias. Based in part on observations obtained with facilities of the Las Cumbres Observatory Global Telescope. Observations reported here were obtained at the MMT Observatory, a joint facility of the Smithsonian Institution and the University of Arizona.

standing the physics that determines the structure of planets.

In Section 2 we summarize the detection of the photometric transit signal and the subsequent spectroscopic and photometric observations of each star to confirm the planets. In Section 3 we analyze the data to rule out false positive scenarios, and to determine the stellar and planetary parameters. Our findings are briefly discussed in Section 4.

2. OBSERVATIONS

The observational procedure employed by HATNet to discover TEPs has been described in detail in several previous discovery papers (e.g. Bakos et al. 2010; Latham et al. 2009). In the following subsections we highlight specific details of the procedure that are relevant to the discoveries of HAT-P-39b through HAT-P-41b.

2.1. *Photometric detection*

Table 1 summarizes the photometric observations of each new planetary system, including the discovery observations made with the HATNet system. The HATNet images were processed and reduced to trend-filtered light curves following the procedure described by Bakos et al. (2010). The light curves were searched for periodic box-shaped signals using the Box Least-Squares (BLS; see Kovács et al. 2002) method. We detected significant signals in the light curves of the stars summarized below (see Figure 1):

- *HAT-P-39* – GSC 1364-01424 (also known as 2MASS 07350197+1749482; $\alpha = 07^{\rm h}35^{\rm m}01.97$s, $\delta = +17^\circ49'48.3''$; J2000; $V = 12.422$, Droege et al. 2006). A signal was detected for this star with an apparent depth of ∼10.9 mmag, and a period of $P = 3.5439$ days.
- *HAT-P-40* – GSC 3607-01028 (also known as 2MASS 22220308+4527265; $\alpha = 22^{\rm h}22^{\rm m}03.00$s, $\delta = +45^\circ27'26.6''$; J2000; $V = 11.699$, Droege et al. 2006). A signal was detected for this star with an apparent depth of ∼4.4 mmag, and a period of $P = 4.4572$ days.
- *HAT-P-41* – GSC 0488-02442 (also known as 2MASS 19491743+0440207; $\alpha = 19^{\rm h}49^{\rm m}17.40$s, $\delta = +04^\circ40'20.7''$; J2000; $V = 11.087$, Droege et al. 2006). A signal was detected for this star with an apparent depth of ∼8.4 mmag, and a period of $P = 2.6940$ days.

2.2. *Reconnaissance Spectroscopy*

High-resolution, low-S/N "reconnaissance" spectra were obtained for HAT-P-39, HAT-P-40, and HAT-P-41 using the Harvard-Smithsonian Center for Astrophysics (CfA) Digital Speedometer (DS; Latham 1992) until it was retired in 2009, and thereafter the Tillinghast Reflector Echelle Spectrograph (TRES; Fűrész 2008), both on the 1.5 m Tillinghast Reflector at the Fred Lawrence Whipple Observatory (FLWO) in AZ. The reconnaissance spectroscopic observations and results for each system are summarized in Table 2. The DS observations

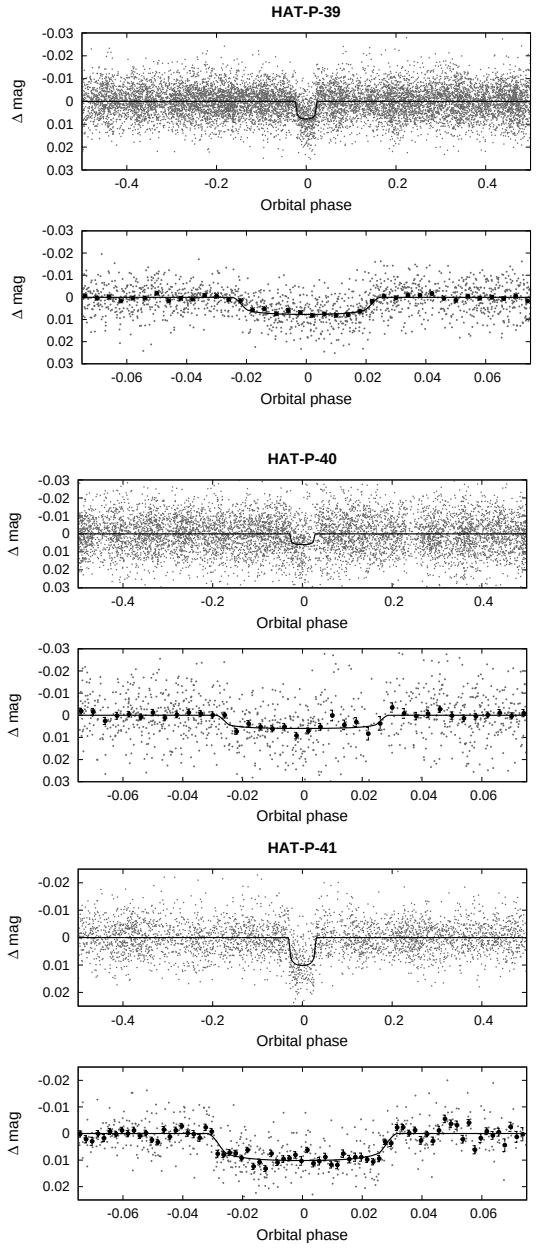

FIG. 1.— HATNet light curves of HAT-P-39 (top), HAT-P-40 (middle) and HAT-P-41 (bottom) phase folded with the transit period. In each case we show two panels: the top shows the unbinned light curve, while the bottom shows the region zoomed-in on the transit, with dark filled circles for the light curve binned in phase with a binsize of 0.002. The solid line shows the model fit to the light curve.

were reduced and analyzed following the procedure described by Torres et al. (2002), while the TRES observations were reduced and analyzed following the procedure described by Quinn et al. (2012) and Buchhave et al. (2010).

Based on the observations summarized in Table 2 we find that all 3 systems have RV root mean square (rms) residuals consistent with no detectable RV variation within the precision of the measurements. All spectra were single-lined, i.e., there is no evidence that any of these targets consist of more than one star. Note that while there is a close companion to HAT-P-41 (Section 2.5), it was resolved by the TRES guider and

TABLE 1
Summary of photometric observations

Instrument/Field	Date(s)	Number of Images	Mode Cadence (min)	Filter
HAT-P-39				
HAT-7/G267	2007 Dec–2008 May	800	5.5	R band
HAT-8/G267	2007 Oct–2008 May	1850	5.5	R band
HAT-6/G315	2007 Dec–2008 May	4700	5.5	R band
HAT-9/G315	2007 Oct–2008 May	2800	5.5	R band
KeplerCam	2009 Mar 30	257	0.89	Sloan i band
KeplerCam	2009 Apr 06	204	0.89	Sloan i band
KeplerCam	2009 Dec 17	373	0.89	Sloan i band
KeplerCam	2011 Feb 12	240	1.0	Sloan i band
HAT-P-40				
HAT-5/G159	2004 Sep–2006 Jan	4403	5.5	I band
HAT-8/G159	2005 Nov–2006 Jan	1591	5.5	I band
HAT-9/G159	2004 Dec–2005 Jan	411	5.5	I band
HAT-11/G159	2004 Dec–2005 Jan	331	5.5	I band
KeplerCam	2010 Sep 16	371	1.40	Sloan i band
FTN	2010 Oct 17	241	0.50	Sloan i band
FTN	2011 Aug 16	285	0.85	Sloan i band
FTN	2011 Aug 25	325	0.94	Sloan i band
FTN	2011 Oct 04	177	0.94	Sloan i band
BOS	2011 Oct 13	381	1.17	Sloan i band
HAT-P-41				
HAT-6/G388	2009 May–2009 Jul	176	5.5	Sloan r band
HAT-8/G388	2009 May–2009 Sep	3380	5.5	Sloan r band
KeplerCam	2010 May 27	226	0.98	Sloan i band
KeplerCam	2010 Jun 23	438	0.49	Sloan i band
KeplerCam	2011 May 31	307	0.73	Sloan i band
KeplerCam	2011 Jun 19	653	0.48	Sloan i band
BOS	2011 Jul 24	238	1.17	Sloan i band

the light from the companion did not go down the fiber. The gravities for all of the stars indicate that none of the stars are giants, though HAT-P-40 may be slightly evolved.

2.3. *High resolution, high S/N spectroscopy*

We proceeded with the follow-up of each candidate by obtaining high-resolution, high-S/N spectra to characterize the RV variations, and to refine the determination of the stellar parameters. The observations were made with HIRES (Vogt et al. 1994) on the Keck-I telescope in Hawaii, and with FIES on the Nordic Optical Telescope on the island of La Palma, Spain (Djupvik & Andersen 2010). We used the high-resolution fiber (providing spectra with a resolution $R = 67{,}000$) for four of the FIES observations, and the medium-resolution fiber ($R = 46{,}000$) for five of the FIES observations. The HIRES observations were reduced to radial velocities in the barycentric frame following the procedure described by Butler et al. (1996), while the FIES observations were reduced following Buchhave et al. (2010). The RV measurements and uncertainties are given in Tables 3-5 for HAT-P-39 through HAT-P-41, respectively. The period-folded data, along with our best fit described below in Section 3 are displayed in Figures 2-4.

In each figure we show also the spectral line bisector spans (BSs) computed from the Keck/HIRES spectra following Torres et al. (2007), the full width at half maximum (FWHM) of the Keck/HIRES spectral lines (computed from the cross-correlation function in a similar manner to the BSs), and the S activity index calculated following Isaacson & Fischer (2010).

2.4. *Photometric follow-up observations*

We conducted additional photometric observations of the three stars with the KeplerCam CCD camera on the FLWO 1.2 m telescope, the Spectral CCD on the 2.0 m Faulkes Telescope North (FTN) at Haleakala Observatory in Hawaii, and the CCD imager on the Byrne Observatory at Sedgwick (BOS) 0.8 m telescope, at Sedgwick Reserve in the Santa Ynez Valley, CA. Both FTN and BOS are operated by the Las Cumbres Observatory Global Telescope (LCOGT[16]; Brown et al. 2012, in preparation). The observations for each target are summarized in Table 1.

The reduction of the KeplerCam images to light curves was performed as described by Bakos et al. (2010). The FTN and BOS images were reduced in a similar manner. We performed EPD and TFA to remove trends simultaneously with the light curve modeling (for more details, see Bakos et al. (2010)). The final time series, together with our best-fit transit light curve model, are shown in the top portion of Figures 5-7, while the individual measurements are reported in Tables 6-8.

2.5. *Adaptive Optics Imaging*

We obtained high-resolution imaging of HAT-P-41 on the night of 21 June 2011 using the Clio2 near-IR imager on the MMT 6.5 m telescope in AZ. Observations were obtained with the adaptive optics (AO) system in H-band and in L'-band. Figure 8 shows the resulting H-band image of HAT-P-41 which easily resolves the $3\farcs56 \pm 0\farcs02$ neighbor.

[16] http://lcogt.net

TABLE 2
Summary of reconnaissance spectroscopy observations

Instrument	$HJD - 2400000$	$T_{\rm eff\star}$ (K)	$\log g_\star$ (cgs)	$v \sin i$ ($\rm km\,s^{-1}$)	$\gamma_{\rm RV}$[a] ($\rm km\,s^{-1}$)
HAT-P-39					
DS	4 obs 54807–54931	6250	4.0	16	28.54 ± 0.58 (rms)
TRES	54934.6546	6500	4.0	16	29.25
HAT-P-40					
TRES	55084.8821	6110 ± 80	4.21 ± 0.13	8.7 ± 0.5	−25.97
TRES	55131.6811	5940 ± 170	4.04 ± 0.26	10.8 ± 1.5	−25.67
TRES	55138.6609	5910 ± 170	3.81 ± 0.27	12.4 ± 1.6	−26.08
TRES	55162.6713	6020 ± 50	3.93 ± 0.10	8.0 ± 0.5	−25.65
TRES	55168.5775	6120 ± 80	4.15 ± 0.14	8.5 ± 0.5	−25.58
HAT-P-41					
TRES	55319.9727	6504 ± 100	4.3 ± 0.16	23.9 ± 0.7	32.32
TRES	55372.9209	5807 ± 223	3.94 ± 0.35	32.1 ± 2.5	29.84
TRES	55373.9046	6430 ± 105	4.28 ± 0.17	27.5 ± 0.7	30.44

[a] The mean heliocentric RV of the target on the IAU system, with a systematic uncertainty of approximately $0.1\,\rm km\,s^{-1}$ mostly limited by how well the velocities of the standard stars have been established. We give the mean and rms RV for the four DS observations of HAT-P-39, the velocity and classification for each TRES observation of HAT-P-39 through HAT-P-41 is listed individually.

TABLE 3
Relative radial velocities, bisector spans, and activity index measurements of HAT-P-39.

BJD[a] (2,454,000+)	RV[b] ($\rm m\,s^{-1}$)	$\sigma_{\rm RV}$[c] ($\rm m\,s^{-1}$)	BS ($\rm m\,s^{-1}$)	$\sigma_{\rm BS}$ ($\rm m\,s^{-1}$)	S[d]	Phase
954.81362	−51.56	7.81	···	···	0.180	0.345
955.84224	32.48	8.82	···	···	0.171	0.635
956.82792	61.50	9.51	···	···	0.175	0.913
1107.13759	−90.39	8.88	−4.63	4.91	0.197	0.327
1109.07573	78.38	9.05	−13.59	7.57	0.183	0.874
1112.12944	42.24	7.88	−4.74	5.19	0.176	0.736
1135.07184	−39.87	6.92	−2.64	4.96	0.178	0.210
1172.95852	−41.57	7.30	19.77	4.58	0.176	0.900
1187.99450	−28.34	8.69	8.74	5.51	···	0.143
1190.10225	70.06	7.12	30.09	4.51	0.181	0.738
1192.03996	−146.19	6.26	16.58	6.61	0.181	0.285
1192.05453	···	···	16.75	3.03	0.180	0.289
1193.05376	−31.04	6.96	−1.15	4.07	0.179	0.571
1193.88084	90.74	7.48	−36.37	5.72	0.178	0.804
1197.00264	89.62	7.37	···	···	0.180	0.685
1198.91700	4.34	10.58	···	···	0.184	0.225
1250.89571	129.15	7.46	−8.86	4.93	0.183	0.892
1251.90337	−98.98	7.98	−6.43	4.96	0.179	0.177
1289.75983	76.11	7.50	−17.19	6.90	0.186	0.859
1312.75610	−14.73	7.40	−17.48	6.40	0.182	0.348
1313.79897	54.76	8.78	2.00	4.22	0.177	0.642
1466.10653	114.14	7.74	2.68	3.75	0.180	0.620
1468.09041	−14.54	6.61	0.53	4.41	0.183	0.180
1470.11601	−11.17	8.91	41.44	5.79	0.174	0.751
1545.08385	27.02	8.10	16.59	4.67	0.179	0.906
1545.86194	−53.41	8.31	1.59	5.47	0.178	0.125
1611.99999	24.36	16.44	−10.80	22.01	0.160	0.788
1698.75509	−64.08	9.64	−22.52	12.11	0.167	0.268
1699.76307	16.59	8.07	−10.35	7.63	0.175	0.553

Note. — Note that for the iodine-free template exposures we do not measure the RV but do measure the BS and S index. Such template exposures can be distinguished by the missing RV value.

[a] Barycentric Julian Date calculated directly from UTC, *without* correction for leap seconds.

[b] The zero-point of these velocities is arbitrary. An overall offset $\gamma_{\rm rel}$ fitted to these velocities in Section 3.3 has *not* been subtracted.

[c] Internal errors excluding the component of astrophysical jitter considered in Section 3.3.

[d] Chromospheric activity index.

TABLE 4
Relative radial velocities, bisector spans, and activity index measurements of HAT-P-40.

BJD[a] (2,454,000+)	RV[b] ($m\,s^{-1}$)	σ_{RV}[c] ($m\,s^{-1}$)	BS ($m\,s^{-1}$)	σ_{BS} ($m\,s^{-1}$)	S[d]	Phase
1191.81591	18.28	3.81	−2.42	4.85	···	0.595
1192.73706	46.75	2.96	−1.85	3.29	0.148	0.802
1192.74599	···	···	4.16	7.06	0.146	0.804
1464.91615	49.92	3.24	−1.75	2.12	0.145	0.867
1465.96736	−41.21	3.02	2.71	4.09	0.144	0.102
1467.92695	17.59	2.93	−9.07	6.74	0.147	0.542
1468.99826	57.77	3.09	2.18	2.51	0.145	0.782
1469.73453	28.31	3.45	−11.76	3.57	0.141	0.948
1486.91164	60.46	3.33	−2.67	6.82	0.145	0.801
1521.81745	35.22	3.96	23.93	6.53	0.143	0.633
1698.11353	−49.94	3.80	4.39	3.60	0.146	0.185
1699.11678	−31.14	3.84	2.58	4.61	0.150	0.410
1701.07726	46.71	3.15	−10.44	4.24	0.145	0.850
1853.75742	−38.93	2.73	···	···	0.148	0.105

Note. — Note that for the iodine-free template exposures we do not measure the RV but do measure the BS and S index. Such template exposures can be distinguished by the missing RV value.
[a] Barycentric Julian Date calculated directly from UTC, *without* correction for leap seconds.
[b] The zero-point of these velocities is arbitrary. An overall offset γ_{rel} fitted to these velocities in Section 3.3 has *not* been subtracted.
[c] Internal errors excluding the component of astrophysical jitter considered in Section 3.3.
[d] Chromospheric activity index.

TABLE 5
Relative radial velocities, bisector spans, and activity index measurements of HAT-P-41.

BJD[a] (2,454,000+)	RV[b] ($m\,s^{-1}$)	σ_{RV}[c] ($m\,s^{-1}$)	BS ($m\,s^{-1}$)	σ_{BS} ($m\,s^{-1}$)	S[d]	Phase	Instrument[e]
1375.97050	92.63	9.38	25.18	6.00	0.155	0.546	Keck
1375.97664	···	···	20.47	5.29	0.155	0.549	Keck
1378.12394	−78.22	9.40	0.84	7.92	0.148	0.346	Keck
1378.58766	52.31	40.10	···	···	···	0.518	FIESm
1379.06917	132.24	9.90	32.40	7.80	0.153	0.697	Keck
1379.54578	21.11	51.30	···	···	···	0.874	FIESm
1380.47420	−106.99	49.00	···	···	···	0.218	FIESm
1381.10708	−39.66	10.23	−1.39	4.57	0.150	0.453	Keck
1381.61687	112.71	49.90	···	···	···	0.642	FIESm
1383.49357	−79.79	75.00	···	···	···	0.339	FIESm
1400.84669	49.04	12.32	−60.12	7.44	0.139	0.780	Keck
1404.80595	−52.53	10.18	−32.58	7.48	0.148	0.250	Keck
1427.51377	112.18	40.10	···	···	···	0.679	FIESh
1428.54090	−22.42	91.50	···	···	···	0.060	FIESh
1429.38087	−79.42	50.00	···	···	···	0.372	FIESh
1431.54013	−153.82	68.60	···	···	···	0.173	FIESh
1465.87835	5.42	11.42	−9.93	6.17	0.145	0.919	Keck
1467.87264	65.94	10.34	−11.95	6.68	0.147	0.659	Keck
1469.89585	−68.65	10.18	17.06	4.94	0.143	0.410	Keck
1490.75265	−113.04	10.38	9.02	9.83	0.145	0.152	Keck
1500.73246	24.76	9.14	12.08	8.78	0.143	0.857	Keck
1704.09441	−67.20	10.27	−1.09	5.26	0.155	0.342	Keck
1814.94017	16.90	10.72	···	···	0.148	0.487	Keck

Note. — Note that for the iodine-free template exposures we do not measure the RV but do measure the BS and S index. Such template exposures can be distinguished by the missing RV value.
[a] Barycentric Julian Date calculated directly from UTC, *without* correction for leap seconds.
[b] The zero-point of these velocities is arbitrary. An overall offset γ_{rel} fitted to these velocities in Section 3.3 has *not* been subtracted.
[c] Internal errors excluding the component of astrophysical jitter considered in Section 3.3.
[d] Chromospheric activity index.
[e] We indicate separately observations obtained with FIES using the medium-resolution fiber, and observations obtained with FIES using the high-resolution fiber.

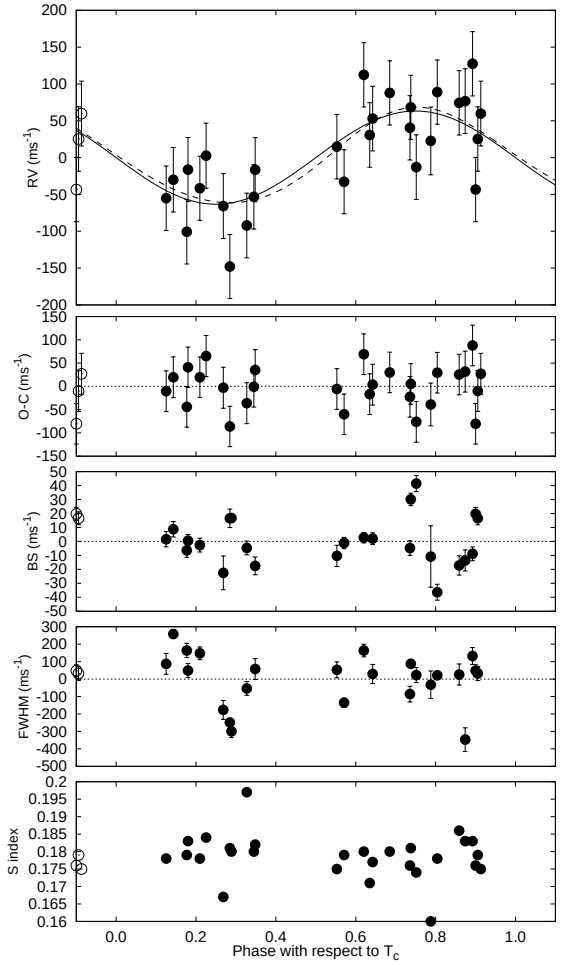

FIG. 2.— *Top panel:* Keck/HIRES RV measurements for HAT-P-39 shown as a function of orbital phase, along with our best-fit circular model (solid line; see Table 11), and our best-fit eccentric model (dashed line). Zero phase corresponds to the time of mid-transit. The center-of-mass velocity has been subtracted. *Second panel:* Velocity $O-C$ residuals from the best fit. The error bars include a component from astrophysical jitter ($43.0\,\mathrm{m\,s^{-1}}$) added in quadrature to the formal errors (see Section 3.3). *Third panel:* Bisector spans (BS), with the mean value subtracted. The measurement from the template spectrum is included. The BS uncertainties are internal errors determined for each spectrum from the scatter of the individual BS values measured on separate orders of the spectrum; they do not include the unknown contribution from stellar jitter. *Fourth panel:* Full width at half maximum (FWHM) of the cross-correlation functions computed from the blue regions of the Keck/HIRES spectra, with the mean value subtracted. *Bottom panel:* Chromospheric activity index S. Note the different vertical scales of the panels. Observations shown twice are represented with open symbols.

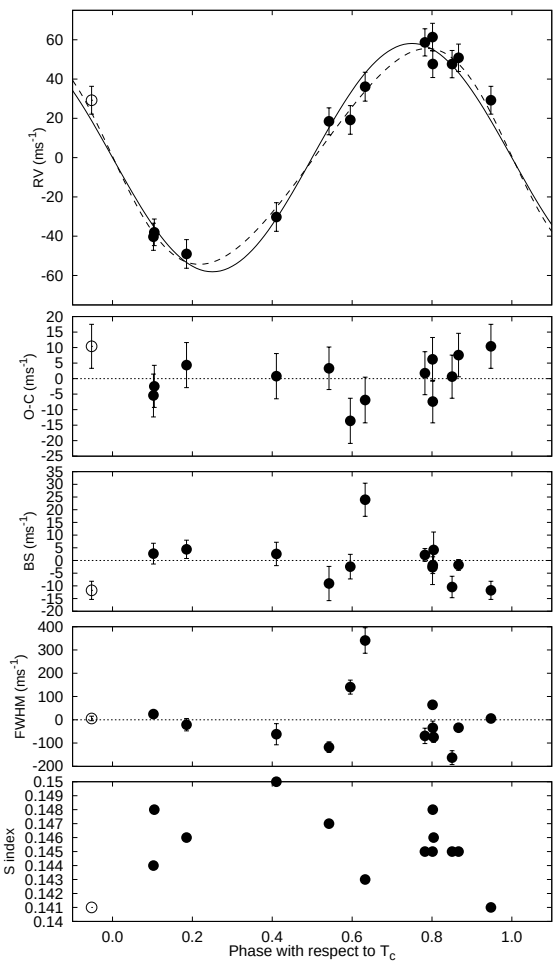

FIG. 3.— Keck/HIRES observations of HAT-P-40. The panels are as in Figure 2. The parameters used in the best-fit model are given in Table 11.

Based on these observations we measure the H- and L'-band magnitudes of the neighbor relative to HAT-P-41 to be $\Delta H = 2.46 \pm 0.06$ mag and $\Delta L' = 2.6 \pm 2.0$ mag. Assuming the star is a physical companion to HAT-P-41, these magnitude differences are consistent with the neighbor being a $\sim 0.7\,M_\odot$ K-dwarf, or roughly ~ 3.5 mag fainter than HAT-P-41 in i band.

The KeplerCam observations of HAT-P-41 described in Section 2.4 show HAT-P-41 to have an elongation in the wing of its PSF due to the companion, but the seeing is not good enough to resolve the stars given the magnitude difference. We use the DAOPHOT and ALLSTAR programs (Stetson 1987, 1992) to obtain PSF-fitting photometry

TABLE 6
HIGH-PRECISION DIFFERENTIAL PHOTOMETRY OF HAT-P-39.

BJD[a] (2,400,000+)	Mag[b]	$\sigma_{\rm Mag}$	Mag(orig)[c]	Filter
54921.62065	0.00694	0.00127	11.10550	i
54921.62127	0.00597	0.00127	11.10530	i
54921.62187	0.00631	0.00126	11.10640	i
54921.62248	0.00358	0.00127	11.10490	i
54921.62311	0.00600	0.00127	11.10610	i
54921.62390	0.00762	0.00127	11.10910	i
54921.62452	0.00787	0.00126	11.10670	i
54921.62512	0.00663	0.00126	11.10860	i
54921.62574	0.01035	0.00126	11.10940	i
54921.62637	0.01050	0.00126	11.11030	i

NOTE. — This table is available in a machine-readable form in the online journal. A portion is shown here for guidance regarding its form and content.

[a] Barycentric Julian Date calculated directly from UTC, *without* correction for leap seconds.

[b] The out-of-transit level has been subtracted. These magnitudes have been subjected to the EPD and TFA procedures, carried out simultaneously with the transit fit.

[c] Raw magnitude values without application of the EPD and TFA procedures.

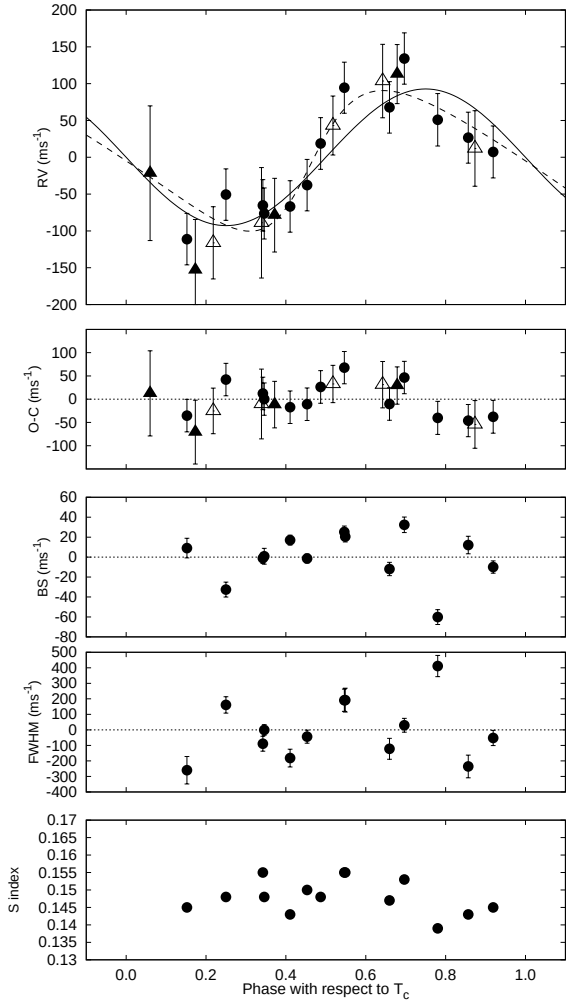

FIG. 4.— Keck/HIRES and FIES/NOT observations of HAT-P-41. The panels are as in Figure 2. Here we use filled circles to show Keck/HIRES observations, filled triangles to show FIES/NOT observations with the high resolution fiber, and open triangles to show FIES/NOT observations with the low resolution fiber. BS and S index measurements are only available for the Keck/HIRES observations. The parameters used in the best-fit model are given in Table 11.

for the two stars, and find that the neighbor is fainter in i band by $\Delta i \approx 3.3$ mag, with an uncertainty of at least 0.1 mag. We conclude that the broad-band photometry is consistent with HAT-P-41 having a K-dwarf binary companion. At the distance of HAT-P-41, the 3.″5 angular separation corresponds to a projected physical separation of ~ 1000 AU between the two stars.

3. ANALYSIS

3.1. *Properties of the parent star*

We measured the stellar atmospheric parameters for each star using the Keck/HIRES Iodine-free template spectra, together with the Spectroscopy Made Easy (SME; Valenti & Piskunov 1996) package, and the Valenti & Fischer (2005) atomic line database. For each star, we obtained the following *initial* values and uncertainties:

- *HAT-P-39* – effective temperature $T_{\rm eff\star} = 6325 \pm 100$ K, metallicity [Fe/H] $= 0.14 \pm 0.1$ dex, stellar surface gravity $\log g_\star = 4.04 \pm 0.1$ (cgs), and pro-

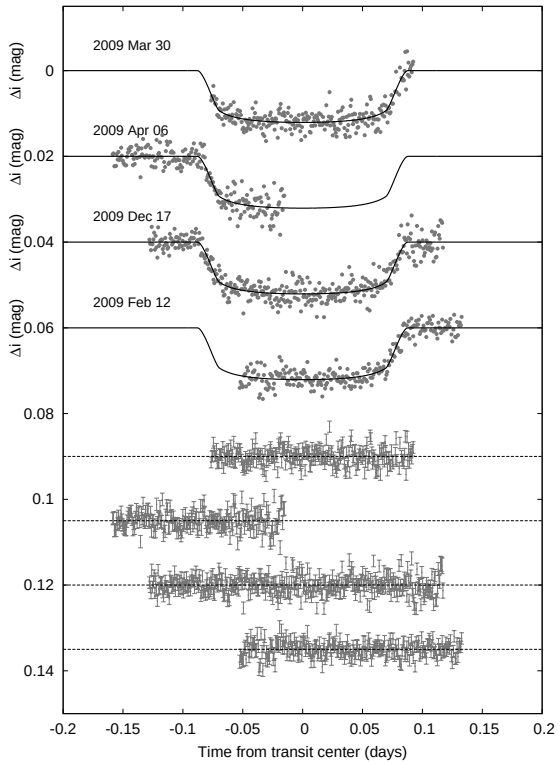

FIG. 5.— Unbinned transit light curves for HAT-P-39, acquired with KeplerCam at the FLWO 1.2 m telescope. The light curves have been EPD- and TFA-processed, as described in § 3.3. The dates of the events are indicated. Curves after the first are displaced vertically for clarity. Our best fit from the global modeling described in Section 3.3 is shown by the solid lines. Residuals from the fits are displayed at the bottom, in the same order as the top curves. The error bars represent the photon and background shot noise, plus the readout noise.

TABLE 7
HIGH-PRECISION DIFFERENTIAL PHOTOMETRY OF HAT-P-40.

BJD[a] (2,400,000+)	Mag[b]	$\sigma_{\rm Mag}$	Mag(orig)[c]	Filter
55456.60581	0.00871	0.00080	10.22060	i
55456.60739	0.00713	0.00067	10.21900	i
55456.60830	0.00854	0.00066	10.22070	i
55456.60930	0.00851	0.00066	10.22100	i
55456.61028	0.00935	0.00065	10.22120	i
55456.61124	0.00789	0.00065	10.21980	i
55456.61224	0.00868	0.00065	10.22070	i
55456.61319	0.00695	0.00065	10.21870	i
55456.61416	0.00727	0.00065	10.21880	i
55456.61513	0.00996	0.00064	10.22200	i

NOTE. — This table is available in a machine-readable form in the online journal. A portion is shown here for guidance regarding its form and content.
[a] Barycentric Julian Date calculated directly from UTC, *without* correction for leap seconds.
[b] The out-of-transit level has been subtracted. These magnitudes have been subjected to the EPD and TFA procedures, carried out simultaneously with the transit fit.
[c] Raw magnitude values without application of the EPD and TFA procedures.

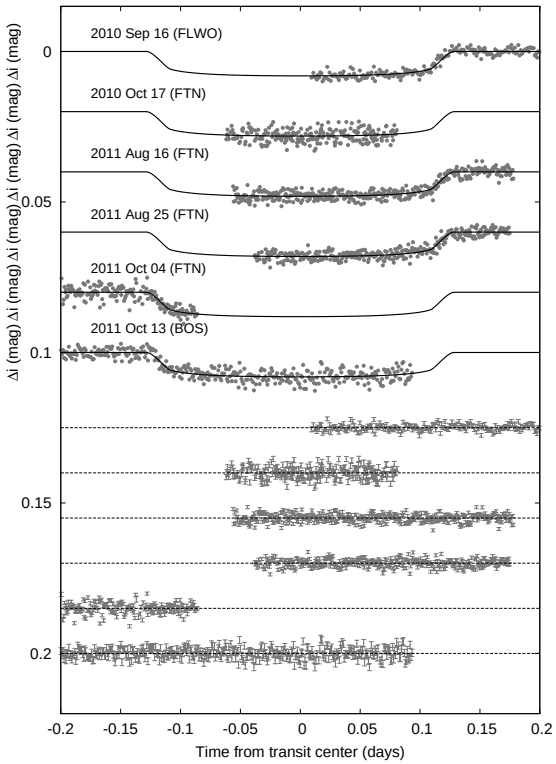

FIG. 6.— Similar to Figure 5; here we show the follow-up light curves for HAT-P-40. The facility used for each each light curve is indicated next to the date of the event.

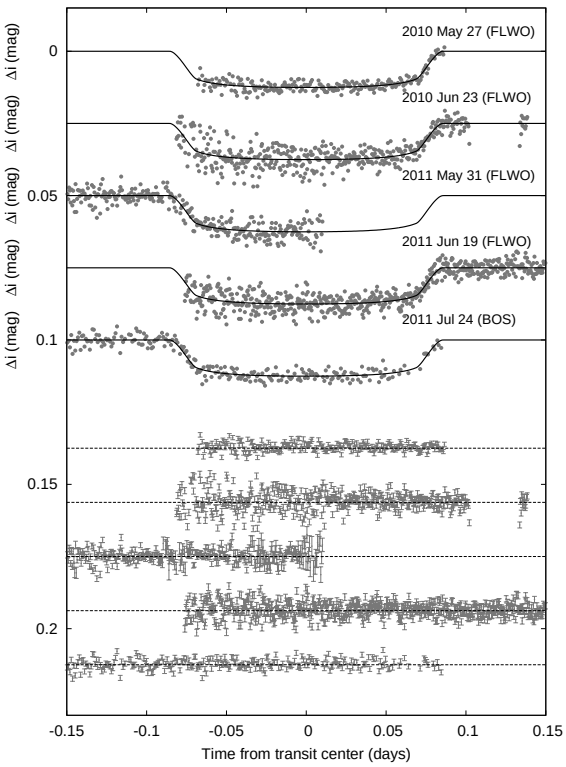

FIG. 7.— Similar to Figure 5; here we show the follow-up light curves for HAT-P-41. The facility used for each each light curve is indicated next to the date of the event.

TABLE 8
HIGH-PRECISION DIFFERENTIAL PHOTOMETRY OF HAT-P-41.

BJD[a] (2,400,000+)	Mag[b]	$\sigma_{\rm Mag}$	Mag(orig)[c]	Filter
55344.79616	0.01161	0.00077	10.01060	i
55344.79679	0.00980	0.00078	10.00870	i
55344.79744	0.00586	0.00078	10.00480	i
55344.79878	0.00847	0.00078	10.00830	i
55344.79946	0.01379	0.00078	10.01310	i
55344.80015	0.01168	0.00078	10.01140	i
55344.80083	0.00987	0.00077	10.00820	i
55344.80151	0.01021	0.00077	10.00830	i
55344.80219	0.01031	0.00076	10.00870	i
55344.80288	0.01025	0.00077	10.00800	i

NOTE. — This table is available in a machine-readable form in the online journal. A portion is shown here for guidance regarding its form and content.
[a] Barycentric Julian Date calculated directly from UTC, *without* correction for leap seconds.
[b] The out-of-transit level has been subtracted. These magnitudes have been subjected to the EPD and TFA procedures, carried out simultaneously with the transit fit.
[c] Raw magnitude values without application of the EPD and TFA procedures.

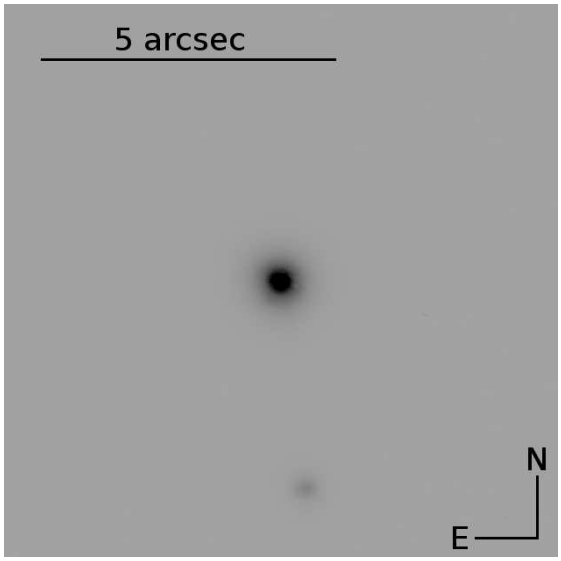

FIG. 8.— H-band AO image of HAT-P-41 obtained with MMT/Clio2 showing the $\sim 3\farcs5$ neighbor to the south.

jected rotational velocity $v \sin i = 12.7 \pm 0.5\,{\rm km\,s^{-1}}$.

- *HAT-P-40* – effective temperature $T_{\rm eff\star} = 6140 \pm 100\,{\rm K}$, metallicity [Fe/H] $= 0.25 \pm 0.1\,{\rm dex}$, stellar surface gravity $\log g_\star = 4.04 \pm 0.1\,({\rm cgs})$, and projected rotational velocity $v \sin i = 6.7 \pm 0.5\,{\rm km\,s^{-1}}$.
- *HAT-P-41* – effective temperature $T_{\rm eff\star} = 6007 \pm 100\,{\rm K}$, metallicity [Fe/H] $= 0.06 \pm 0.1\,{\rm dex}$, stellar surface gravity $\log g_\star = 3.68 \pm 0.06\,({\rm cgs})$, and projected rotational velocity $v \sin i = 20.6 \pm 0.5\,{\rm km\,s^{-1}}$.

As described in our previous papers (e.g. Bakos et al. 2010), these initial values were used to determine the quadratic limb-darkening coefficients for each star from the Claret (2004) tables. We then used the mean stellar density, determined from the normalized semimajor axis $a/R_\star$, together with the effective temperature and metallicity to determine an initial estimate of the mass and

radius of each star from the Yonsei-Yale (YY) isochrones (Yi et al. 2001). This provided a refined estimate of the stellar surface gravity, which we fixed in a second iteration of SME for each star. For each system a third iteration did not change $\log g_\star$ appreciably, so we adopted the values from the second iteration as the final spectroscopic parameters for each star. These parameters are listed in Table 9. In this same table we also list the available broad-band photometric magnitudes from the literature, and physical parameters, such as the stellar masses and radii, which are determined from the spectroscopic parameters together with the model isochrones. As discussed in Section 3.3 we adopt the parameters assuming a circular orbit for each planet. Some of the parameters, especially the derived stellar masses and radii, depend on the eccentricity; Table 10 lists the values for these parameters when the eccentricity is allowed to vary.

The inferred location of each star in a diagram of $a/R_\star$ versus $T_{\rm eff\star}$, analogous to the classical H-R diagram, is shown in Figure 9. In each case the stellar properties and their 1σ and 2σ confidence ellipsoids are displayed against the backdrop of model isochrones for a range of ages, and the appropriate stellar metallicity. For comparison, the locations implied by the initial SME results are also shown (in each case with a triangle).

We determine the distance and extinction to each star by comparing the J, H and K_S magnitudes from the 2MASS Catalogue (Skrutskie et al. 2006), and the V and I_C magnitudes from the TASS Mark IV Catalogue (Droege et al. 2006), to the expected magnitudes from the stellar models. We use the transformations by Carpenter (2001) to convert the 2MASS magnitudes to the photometric system of the models (ESO), and use the Cardelli et al. (1989) extinction law, assuming a total-to-selective extinction ratio of $R_V = 3.1$, to relate the extinction in each band-pass to the V-band extinction A_V. The resulting A_V and distance measurements are given in Table 9. We find total V band extinctions of $A_V = 0.171 \pm 0.135$, 0.353 ± 0.127, and 0.248 ± 0.134 mag for HAT-P-39 through HAT-P-41, respectively. For comparison, the total line of sight extinctions in each direction, estimated from the Schlegel et al. (1998) dust maps, are: 0.146 mag, 0.724 mag, and 0.513 mag. Following Bonifacio et al. (2000), we estimate the expected distance-corrected extinction to each source to be 0.113 mag, 0.306 mag, and 0.157 mag, respectively. For HAT-P-39 and HAT-P-40 the measured and expected values are consistent. For HAT-P-41 the broad-band photometry appears to point to a slightly redder star than expected based on the spectroscopic temperature and expected extinction. As noted in Section 2.5, HAT-P-41 has a close companion which is unresolved in the 2MASS or TASS catalogs, this companion is the probable cause of the discrepancy between the expected and observed magnitudes of HAT-P-41.

3.2. *Excluding blend scenarios*

The analyses of our reconnaissance spectroscopic observations discussed in Section 2.2 rule out the most obvious astrophysical false positive scenarios for HAT-P-39 through HAT-P-41. Additionally the spectral-line bisector span (BS) analyses which we conducted (Figures 2-4) provide constraints on more subtle blend scenarios similar to that presented in Torres et al. (2004). However, because HAT-P-39 and HAT-P-41 have high RV jitter, and consequently high BS scatter ($\sim 80\,{\rm m\,s^{-1}}$ and $\sim 30\,{\rm m\,s^{-1}}$, respectively), relative to their RV semiamplitudes ($63.6 \pm 10.4\,{\rm m\,s^{-1}}$ and $92.5 \pm 11.6\,{\rm m\,s^{-1}}$, respectively), the BS test provides a less stringent constraint on possible blend scenarios than it does in a case such as HAT-P-40 (BS scatter of $\sim 10\,{\rm m\,s^{-1}}$ and RV semi-amplitude of $58.1 \pm 2.9\,{\rm m\,s^{-1}}$). To provide additional support for the planetary interpretation of the observations of each system we conduct detailed blend analyses of the light curves (including both the HATNet discovery light curves, and all available follow-up light curves) and absolute photometry following Hartman et al. (2011).

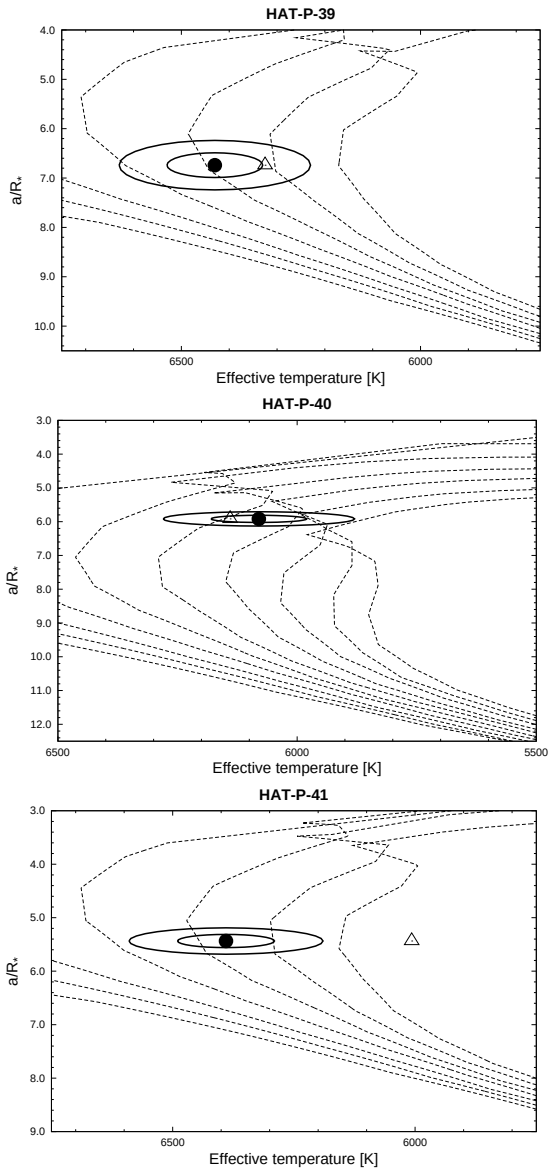

FIG. 9.— Model isochrones from Yi et al. (2001) for the metallicities of HAT-P-39 (top), HAT-P-40 (center) and HAT-P-41 (bottom). For HAT-P-39 and HAT-P-41 the isochrones are shown for ages of 0.2 Gyr, 0.6 Gyr, and 1.0 Gyr to 3.0 Gyr in steps of 0.5 Gyr (left to right), while for HAT-P-40 the isochrones are shown for ages of 0.2 Gyr, 0.6 Gyr and 1.0 Gyr to 4.5 Gyr in steps of 0.5 Gyr (left to right). The adopted values of $T_{\rm eff\star}$ and $a/R_\star$ are shown together with their 1σ and 2σ confidence ellipsoids. In each plot the initial values of $T_{\rm eff\star}$ and $a/R_\star$ from the first SME and light curve analyses are represented with a triangle.

TABLE 9
Adopted stellar parameters for HAT-P-39–HAT-P-41 assuming circular orbits

Parameter	**HAT-P-39** Value	**HAT-P-40** Value	**HAT-P-41** Value	Source
Spectroscopic properties				
$T_{\rm eff\star}$ (K)	6430 ± 100	6080 ± 100	6390 ± 100	SME[a]
[Fe/H]	0.19 ± 0.10	0.22 ± 0.10	0.21 ± 0.10	SME
$v \sin i$ (km s^{-1})	12.7 ± 0.5	6.9 ± 0.5	19.6 ± 0.5	SME
$v_{\rm mac}$ (km s^{-1})	5.04	4.50	4.97	SME
$v_{\rm mic}$ (km s^{-1})	0.85	0.85	0.85	SME
$\gamma_{\rm RV}$ (km s^{-1})	28.42 ± 0.28	-25.0 ± 0.1	31.68 ± 0.61	DS or TRES
Photometric properties				
V (mag)	12.422	11.699	11.087	TASS
$V-I_C$ (mag)	0.58 ± 0.15	0.77 ± 0.12	0.63 ± 0.10	TASS
J (mag)	11.424 ± 0.020	10.367 ± 0.023	10.006 ± 0.027	2MASS
H (mag)	11.184 ± 0.022	10.085 ± 0.018	9.777 ± 0.032	2MASS
K_s (mag)	11.157 ± 0.020	10.009 ± 0.018	9.728 ± 0.029	2MASS
Derived properties				
$M_\star$ ($M_\odot$)	1.404 ± 0.051	$1.512^{+0.045}_{-0.109}$	1.418 ± 0.047	YY+$a/R_\star$+SME[b]
$R_\star$ ($R_\odot$)	$1.625^{+0.081}_{-0.062}$	2.206 ± 0.061	$1.683^{+0.058}_{-0.036}$	YY+$a/R_\star$+SME
$\log g_\star$ (cgs)	4.16 ± 0.03	3.93 ± 0.02	4.14 ± 0.02	YY+$a/R_\star$+SME
$L_\star$ ($L_\odot$)	4.05 ± 0.48	6.00 ± 0.61	4.25 ± 0.41	YY+$a/R_\star$+SME
M_V (mag)	3.21 ± 0.14	2.83 ± 0.13	3.16 ± 0.12	YY+$a/R_\star$+SME
M_K (mag,ESO)	2.12 ± 0.10	1.49 ± 0.07	2.04 ± 0.06	YY+$a/R_\star$+SME
Age (Gyr)	2.0 ± 0.4	$2.7^{+0.9}_{-0.3}$	2.2 ± 0.4	YY+$a/R_\star$+SME
A_V (mag)[c]	0.171 ± 0.135	0.353 ± 0.127	0.248 ± 0.134	YY+$a/R_\star$+SME
Distance (pc)	642 ± 29	501 ± 16	344^{+12}_{-8}	YY+$a/R_\star$+SME
$\log R'_{\rm HK}$[d]	-4.85 ± 0.07	-5.12 ± 0.16	-5.04 ± 0.04	Keck/HIRES

[a] SME = "Spectroscopy Made Easy" package for the analysis of high-resolution spectra (Valenti & Piskunov 1996). These parameters rely primarily on SME, but have a small dependence also on the iterative analysis incorporating the isochrone search and global modeling of the data, as described in the text.
[b] YY+$a/R_\star$+SME = Based on the YY isochrones (Yi et al. 2001), $a/R_\star$ as a luminosity indicator, and the SME results.
[c] V band extinction determined by comparing the measured 2MASS and TASS photometry for the star to the expected magnitudes from the YY+$a/R_\star$+SME model for the star. We use the Cardelli et al. (1989) extinction law.
[d] Chromospheric activity index defined in Noyes et al. (1984) determined from the Keck/HIRES spectra following Isaacson & Fischer (2010). In each case we give the average value and the standard deviation from the individual spectra.

TABLE 10
Derived stellar parameters for HAT-P-39–HAT-P-41 allowing eccentric orbits[a]

Parameter	**HAT-P-39** Value	**HAT-P-40** Value	**HAT-P-41** Value	Source
$M_\star$ ($M_\odot$)	$1.400^{+0.102}_{-0.069}$	1.504 ± 0.103	1.405 ± 0.066	YY+$a/R_\star$+SME
$R_\star$ ($R_\odot$)	$1.622^{+0.294}_{-0.167}$	2.422 ± 0.154	$1.525^{+0.177}_{-0.133}$	YY+$a/R_\star$+SME
$\log g_\star$ (cgs)	4.16 ± 0.10	3.85 ± 0.04	4.22 ± 0.07	YY+$a/R_\star$+SME
$L_\star$ ($L_\odot$)	$4.01^{+1.78}_{-0.81}$	$6.98^{+1.27}_{-0.97}$	$3.68^{+1.00}_{-0.68}$	YY+$a/R_\star$+SME
M_V (mag)	3.22 ± 0.31	2.67 ± 0.18	3.31 ± 0.25	YY+$a/R_\star$+SME
M_K (mag,ESO)	2.12 ± 0.29	1.31 ± 0.14	2.25 ± 0.22	YY+$a/R_\star$+SME
Age (Gyr)	$2.0^{+0.5}_{-0.6}$	$2.9^{+0.8}_{-0.6}$	1.5 ± 0.6	YY+$a/R_\star$+SME
A_V (mag)	$0.156^{+0.152}_{-0.111}$	0.317 ± 0.126	0.332 ± 0.134	YY+$a/R_\star$+SME
Distance (pc)	641^{+115}_{-66}	548 ± 36	311^{+36}_{-27}	YY+$a/R_\star$+SME

[a] Quantities and abbreviations are as in Table 9, which gives our adopted values, determined assuming circular orbits. We do not list parameters that are independent of the eccentricity.

In Figure 10 we show, for each system, the histogram of $\Delta\chi^2$ values between the best-fit transiting planet model and the best-fit blend model for simulated data sets having the same noise properties as the observed residuals from the best-fit blend model (see Hartman et al. 2011 for a more detailed discussion). In this same figure we also show the $\Delta\chi^2$ difference between the best-fit models applied to the observations. We find that for HAT-P-39 and HAT-P-41 we can reject blend scenarios involving combinations of three stars with greater than 3σ and 5σ confidence, respectively, based solely on the photometry. For HAT-P-39 the detailed shape of the transit, as determined from the follow-up light curves, contributes most of the χ^2 difference between the models, while for HAT-P-41 it is the lack of out-of-transit variations, as determined from the HATNet light curve, that contributes most of the χ^2 difference. For HAT-P-40 we are unable to rule out blend scenarios based solely on the photometry, however in this case the lack of BS or FWHM variations rules out such blends. To quantify this, we simulate the cross-correlation function (CCF) of blended systems which could plausibly fit the photometric data (configurations which cannot be rejected with greater than 5σ confidence) and find that in all cases either the RV or FWHM of the blended configuration varies by several $\mathrm{km\,s^{-1}}$, or the BS varies by greater than $\sim 100\,\mathrm{m\,s^{-1}}$, greatly exceeding the observational limits on any such variations. Similarly for HAT-P-39 we find that stellar blend configurations which cannot be rejected with greater than 5σ confidence predict greater than $500\,\mathrm{m\,s^{-1}}$ variations in the RV or BS of the Keck spectra, which are well above the observational constraints.

As discussed in Section 2.5, HAT-P-41 has a close neighbor which we estimate to be ~ 3.5 mag fainter in i band. While such a neighbor could, in principle, be eclipsed by an object that would produce a $\sim 1\%$ dip in the blended light curve, as we have shown here, the detailed shape of the light curve cannot be produced using physically possible combinations of stars (i.e. stars with parameters determined from stellar evolution models). We note that the KeplerCam observations show no evidence for variations in the flux centroid that correlate with the photometry, providing further evidence that the observed variation is not due to a deep eclipse in the poorly resolved neighbor.

While we can rule out, for each of the systems, blend scenarios involving only stellar-mass components, we cannot rule out scenarios involving binary star systems with one component hosting a transiting planet. Indeed, for HAT-P-41 we find that including a $\sim 0.7\,M_\odot$ star in the system provides a slightly better fit to the photometric observations. In this case we actually know that there is a faint companion (though it is unresolved in our light curves or the available absolute broad-band photometry measurements), so it is reassuring to find that the blend analysis of the photometric data also points to the existence of this companion. For HAT-P-39 we can rule out binary companion stars with $M < 1.24\,M_\odot$ while for HAT-P-40 and HAT-P-41 we cannot rule out binary companions of any mass up to that of the mass inferred for the brighter star in the system. While massive binary companions in general should be easier to detect in the spectrum, if the two stars have very similar average velocities, the resulting variations in BS, FWHM, and RV measurements can be less than the constraints set by the observations.

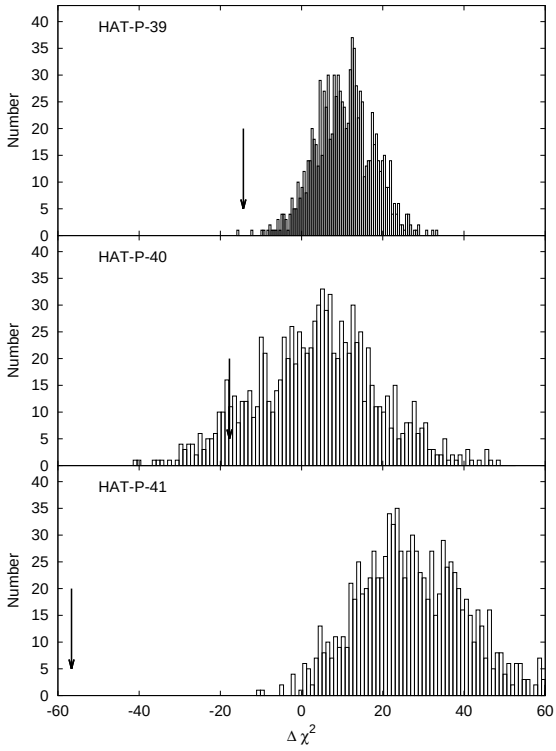

FIG. 10.— The histogram of $\Delta\chi^2$ values between the best-fit transiting planet model and the best-fit blend model for simulated data sets having the same noise properties as the observed residuals from the best-fit blend model (see Hartman et al. 2011 for a more detailed discussion). The histogram is shown separately for each system. In each panel the arrow shows the χ^2 difference between the models fitted to the actual observations. For HAT-P-41 the best-fit blend scenario is rejected based on the photometry with greater than 5σ confidence. For HAT-P-39 and HAT-P-40, blend scenarios which cannot be rejected based solely on the photometry are rejected based on spectroscopic information (limits on variations in RV, and in the BS and FWHM of the spectral line profiles).

We conclude that each system presented here contains a transiting planet, however we cannot definitively claim that these are all single stars. There is no evidence that either HAT-P-39 or HAT-P-40 is a binary system, so we treat each of these as single stars in the analysis that follows. For HAT-P-41 there is a resolved neighbor which we account for in our analysis of the system.

3.3. *Global modeling of the data*

We modelled the HATNet photometry, the follow-up photometry, and the high-precision RV measurements using the procedure described by Bakos et al. (2010). Following the discussion by Eastman et al. (2012), we made two important changes to our analysis procedure compared to what was done in Bakos et al. (2010). As noted in section 3.5.3 of Eastman et al. (2012), there is a common mistake in the implementation of the Metropolis-Hastings (M-H) algorithm for conducting a Markov Chain Monte Carlo (MCMC) analysis whereby the Markov chain is not increased when a proposed transition is rejected. We discovered that the implementation we have been using for the analysis of HATNet planets

has made this mistake, and have corrected it for the analysis of the planets presented in this paper. We found that this bug tends to inflate the errorbars on the determined parameters by a factor of a few parts in a hundred. Errors given in previous discovery papers may thus be slightly overestimated. The second significant change that we have made is to use $\sqrt{e}\cos\omega$ and $\sqrt{e}\sin\omega$ as jump parameters, rather than $e\cos\omega$ and $e\sin\omega$. Previously we had been assuming uniform priors on the latter jump parameters, which amounts to assuming a linear prior on the eccentricity e, creating a bias towards measuring nonzero eccentricities. As other authors have noted, using $\sqrt{e}\cos\omega$ and $\sqrt{e}\sin\omega$ leads to a uniform prior on e. We found that this change had a much more significant impact on our determined parameters than did correcting the bug in our implementation of M-H. For example, for HAT-P-39b the eccentricity that we find is 0.094 ± 0.086 compared with 0.161 ± 0.094 when using our old jump parameters.

We also made a few minor changes to the analysis for the particular planets presented in this paper. For the analysis of HAT-P-41 we allowed independent RV zero-points for the Keck/HIRES RVs, the high-resolution NOT/FIES RVs, and the medium-resolution NOT/FIES RVs. To account for the contribution from the neighbor to the photometry, we also fixed the third light in the i band to 4%, based on our PSF-fitting analysis of the KeplerCam observations of this system.

For each planet we performed the fit both allowing eccentricity to vary and fixing it to zero. The resulting parameters for each system are listed in Table 11, assuming circular orbits, and in Table 12 allowing eccentric orbits. We use a Lucy & Sweeney (1971) test to determine the significance of the measured eccentricities of each system. We find that the observations of all three systems are consistent with the planets being on circular orbits (the circular orbit hypothesis is rejected with 45% confidence, 86% confidence, and 91% confidence, for HAT-P-39b, HAT-P-40b and HAT-P-41b, respectively; for reference the confidence level would need to be greater than 99.7% for the detection of a nonzero eccentricity to be significant at the 3σ level, which is generally taken as a minimum level of significance). In the past we have generally presented parameters for systems allowing the eccentricity to vary, even in cases where the observations are consistent with a circular orbit, on the grounds that this provides a more conservative estimate of the errors. However, as discussed recently by Anderson et al. (2012), the best-fit parameters which result from allowing the eccentricity to vary are often biased relative to the circular orbit values, and in most cases further follow-up observations, such as occultation observations, reveal the planets to be on circular orbits after all. We therefore suggest adopting the circular orbit parameters as the most probable values for each planet. These are given in Table 11. For reference Table 12 lists the resulting parameters when the eccentricities are varied.

4. DISCUSSION

We have presented the discovery of three new transiting planets which we show on mass–radius and equilibrium temperature–radius diagrams in Figure 11. As seen in the mass–radius diagram planets generally have radii with $0.6\,R_{\rm J} < R < 1.5\,R_{\rm J}$ over a broad mass-range spanning over two orders of magnitude, except for in the range $0.4\,M_{\rm J} < M < 1.5\,M_{\rm J}$ where planets are found with radii as large as $\sim 2.0\,R_{\rm J}$ (if WASP-12b is excluded, then the mass range is $0.4\,M_{\rm J} < M < 1.0\,M_{\rm J}$). Applying the Kolmogorov-Smirnov test (e.g. Press et al. 1992), we find that there is only a 0.7% chance that the masses of planets with $M > 0.4\,M_{\rm J}$ and $R > 1.5\,R_{\rm J}$ are drawn from the same distribution as the masses of planets with $M > 0.4\,M_{\rm J}$ and $R < 1.5\,R_{\rm J}$. The three planets presented here fall in the population of large radius ($R > 1.5\,R_{\rm J}$), sub-Jupiter-mass planets which we refer to as highly inflated planets.

As has been repeatedly noted (the earliest reference being Guillot 2005) the radii of close-in gas-giant planets are strongly correlated with the degree of irradiation (variously traced by the planet equilibrium temperature estimated by adopting a constant albedo, typically zero, for all planets, and making an assumption about the heat redistribution, or traced by the bolometric surface flux). As is evident in Figure 11, the degree to which planets are inflated depends on their masses, with lower mass planets showing a stronger correlation between temperature and radius. This has also been previously noted (e.g. Enoch et al. 2012) and has been taken as evidence for some theoretical models of the inflation process (e.g. Batygin et al. 2011; Laughlin et al. 2011). The planets presented here generally follow the established empirical trends, though they are somewhat more inflated than other planets with comparable equilibrium temperatures and semimajor axes. The empirical relation given by Enoch et al. (2012), which gives a prediction for the radius as a function of $T_{\rm eq}$ and a for planets with $0.5\,M_{\rm J} < M_p < 2.0\,M_{\rm J}$, yields radii of $1.52\,R_{\rm J}$, $1.63\,R_{\rm J}$, and $1.58\,R_{\rm J}$ for HAT-P-39b through HAT-P-41b, respectively. The formula given by Béky et al. (2011), which uses $T_{\rm eq}$ and [Fe/H] as indepedent variables and was derived for planets with $0.3\,M_{\rm J} < M_p < 0.8\,M_{\rm J}$ predicts radii of $1.31\,R_{\rm J}$, $1.30\,R_{\rm J}$ and $1.37\,R_{\rm J}$. In all cases the predicted radii are smaller than the measured values ($1.57\,R_{\rm J}$, $1.73\,R_{\rm J}$, and $1.68\,R_{\rm J}$), though the Enoch et al. (2012) relation, which was determined including more recent discoveries, gives values that are closer to the observations.

We find that HAT-P-41 has a neighbor which has near-IR photometry consistent with it being a $0.7\,M_{\odot}$ star at the same distance as HAT-P-41. HAT-P-41 is thus one of number of hot Jupiter host stars with close visually-resolved neighbors (e.g. HD 189733, Bakos et al. 2006; HAT-P-1, Bakos et al. 2007; and many others), though it is not known what fraction of these are physical companions. Such companions may be responsible for driving planets into close-in orbits via the Kozai Mechanism (Fabrycky & Tremaine 2007), a hypothesis which has gained traction recently with the discovery that many close-in planets are on high obliquity orbits (e.g. Triaud et al. 2010; Albrecht et al. 2012), but a complete survey to determine the frequency of companions to hot Jupiter host stars in a statistically robust way has not yet been published.

Finally we note that all three of these planets are good targets for measuring the Rossiter-McLaughlin effect (R-M; Rossiter 1924; McLaughlin 1924) as they orbit bright stars with relatively high projected rotation velocities. For HAT-P-39b and HAT-P-41b the expected R-M semi-

TABLE 11
Adopted orbital and planetary parameters for HAT-P-39b–HAT-P-41b assuming circular orbits

Parameter	**HAT-P-39b** Value	**HAT-P-40b** Value	**HAT-P-41b** Value
Light curve parameters			
P (days)	3.543870 ± 0.000005	4.457243 ± 0.000010	2.694047 ± 0.000004
T_c (BJD) [a]	$2455208.75049 \pm 0.00041$	$2455813.17584 \pm 0.00054$	$2454983.86167 \pm 0.00107$
T_{14} (days) [a]	0.1745 ± 0.0017	0.2557 ± 0.0014	0.1704 ± 0.0012
$T_{12} = T_{34}$ (days) [a]	0.0178 ± 0.0017	0.0196 ± 0.0009	0.0166 ± 0.0009
$a/R_\star$	6.74 ± 0.25	$5.92^{+0.06}_{-0.14}$	$5.44^{+0.09}_{-0.15}$
$\zeta/R_\star$ [b]	12.75 ± 0.07	8.48 ± 0.04	13.01 ± 0.06
$R_p/R_\star$	0.0993 ± 0.0025	0.0807 ± 0.0014	0.1028 ± 0.0016
b^2	$0.122^{+0.069}_{-0.061}$	$0.030^{+0.045}_{-0.019}$	$0.049^{+0.051}_{-0.029}$
$b \equiv a\cos i/R_\star$	$0.349^{+0.085}_{-0.120}$	$0.174^{+0.091}_{-0.077}$	$0.222^{+0.088}_{-0.093}$
i (deg)	87.0 ± 1.0	88.3 ± 0.9	87.7 ± 1.0
Limb-darkening coefficients [c]			
c_1, i (linear term)	0.1787	0.2190	0.1908
c_2, i (quadratic term)	0.3812	0.3650	0.3746
c_1, r	···	···	0.2658
c_2, r	···	···	0.3814
c_1, I	···	0.1987	···
c_2, I	···	0.3646	···
c_1, R	0.2335	···	···
c_2, R	0.3871	···	···
RV parameters			
K ($\mathrm{m\,s^{-1}}$)	63.6 ± 10.4	58.1 ± 2.9	92.5 ± 11.6
e	0 (fixed)	0 (fixed)	0 (fixed)
RV jitter ($\mathrm{m\,s^{-1}}$)[d]	43.0	6.2	33.4
Planetary parameters			
M_p (M_J)	0.599 ± 0.099	0.615 ± 0.038	0.800 ± 0.102
R_p (R_J)	$1.571^{+0.108}_{-0.081}$	1.730 ± 0.062	$1.685^{+0.076}_{-0.051}$
$C(M_p, R_p)$ [e]	0.09	0.36	0.10
ρ_p ($\mathrm{g\,cm^{-3}}$)	0.19 ± 0.04	0.15 ± 0.01	0.20 ± 0.03
$\log g_p$ (cgs)	2.77 ± 0.09	2.71 ± 0.03	2.84 ± 0.06
a (AU)	0.0509 ± 0.0006	$0.0608^{+0.0006}_{-0.0015}$	0.0426 ± 0.0005
T_eq (K)[f]	1752 ± 43	1770 ± 33	1941 ± 38
Θ[g]	0.027 ± 0.005	0.029 ± 0.002	0.028 ± 0.004
$\langle F \rangle$ ($10^9 \mathrm{erg\,s^{-1}\,cm^{-2}}$) [h]	2.13 ± 0.21	2.22 ± 0.17	3.20 ± 0.25

[a] Reported times are in Barycentric Julian Date calculated directly from UTC, *without* correction for leap seconds. T_c: Reference epoch of mid transit that minimizes the correlation with the orbital period. T_{14}: total transit duration, time between first to last contact; $T_{12} = T_{34}$: ingress/egress time, time between first and second, or third and fourth contact.

[b] Reciprocal of the half duration of the transit used as a jump parameter in our MCMC analysis in place of $a/R_\star$. It is related to $a/R_\star$ by the expression $\zeta/R_\star = a/R_\star(2\pi(1 + e\sin\omega))/(P\sqrt{1-b^2}\sqrt{1-e^2})$ (Bakos et al. 2010).

[c] Values for a quadratic law, adopted from the tabulations by Claret (2004) according to the spectroscopic (SME) parameters listed in Table 9.

[d] Error term, either astrophysical or instrumental in origin, added in quadrature to the formal Keck/HIRES RV errors such that χ^2 per degree of freedom is unity. For HAT-P-41 we did not add a jitter term to the FIES/NOT RV errors because the formal errors for these observations exceeded the scatter in the RV residuals.

[e] Correlation coefficient between the planetary mass M_p and radius R_p.

[f] Planet equilibrium temperature averaged over the orbit, calculated assuming a Bond albedo of zero, and that flux is reradiated from the full planet surface.

[g] The Safronov number is given by $\Theta = \frac{1}{2}(V_\mathrm{esc}/V_\mathrm{orb})^2 = (a/R_p)(M_p/M_\star)$ (see Hansen & Barman 2007).

[h] Incoming flux per unit surface area, averaged over the orbit.

amplitude is over $100\,\mathrm{m\,s^{-1}}$. For HAT-P-40b the signal amplitude is lower, but this is compensated by the long duration of the transit. The three stars are also positioned closely below (HAT-P-40) and above (HAT-P-39 and HAT-P-41) the 6250 K effective temperature threshold found by Winn et al. (2010) to separate planets on orbits that are well aligned with the spin axes of their host stars from planets that are on high obliquity orbits (see also Albrecht et al. 2012).

Acknowledgements— HATNet operations have been funded by NASA grants NNG04GN74G, NNX08AF23G and SAO IR&D grants. J.H. acknowledges partial support from NSF grant AST-1108686. G.Á.B., Z.C. and K.P. acknowledge partial support from NASA grant NNX09AB29G. GT acknowledges partial support from NASA grant NNX09AF59G. We acknowledge partial support also from the Kepler Mission under NASA Cooperative Agreement NCC2-1390 (D.W.L., PI). G.K. thanks the Hungarian Scientific Research Foundation (OTKA) for support through grant K-81373. This research has made use of Keck telescope time granted through NOAO (A201Hr, A289Hr, A284Hr), NASA (N049Hr, N018Hr, N167Hr, N029Hr, N108Hr,

TABLE 12
Orbital and planetary parameters for HAT-P-39b–HAT-P-41b allowing eccentric orbits[a]

Parameter	**HAT-P-39b** Value	**HAT-P-40b** Value	**HAT-P-41b** Value
Light curve parameters			
$a/R_\star$	6.74 ± 0.77	5.39 ± 0.28	5.97 ± 0.52
$\zeta/R_\star$	12.76 ± 0.08	8.49 ± 0.04	12.99 ± 0.06
i (deg)	$87.1^{+1.1}_{-1.5}$	$88.0^{+0.9}_{-1.2}$	87.9 ± 0.9
RV parameters			
K ($\mathrm{m\,s^{-1}}$)	63.8 ± 10.6	55.4 ± 2.5	95.6 ± 10.4
$\sqrt{e}\cos\omega$	0.094 ± 0.189	0.041 ± 0.064	-0.189 ± 0.100
$\sqrt{e}\sin\omega$	-0.008 ± 0.263	$0.300^{+0.074}_{-0.137}$	$-0.293^{+0.244}_{-0.120}$
$e\cos\omega$	0.022 ± 0.074	0.012 ± 0.018	-0.068 ± 0.039
$e\sin\omega$	-0.001 ± 0.114	0.092 ± 0.051	-0.105 ± 0.086
e	0.094 ± 0.086	0.095 ± 0.048	0.139 ± 0.063
ω (deg)	188 ± 115	83 ± 42	237 ± 38
RV jitter ($\mathrm{m\,s^{-1}}$)	42.7	4.1	27.5
Secondary eclipse parameters			
T_s (BJD)	2455189.310 ± 0.168	2455819.895 ± 0.052	2454985.092 ± 0.068
$T_{s,14}$	0.1741 ± 0.0378	0.3048 ± 0.0300	0.1397 ± 0.0241
$T_{s,12}$	0.0176 ± 0.0084	0.0239 ± 0.0029	0.0135 ± 0.0027
Planetary parameters			
M_p (M_J)	0.596 ± 0.099	0.584 ± 0.035	0.812 ± 0.094
R_p (R_J)	$1.565^{+0.292}_{-0.169}$	1.900 ± 0.127	$1.529^{+0.185}_{-0.136}$
$C(M_p, R_p)$	0.08	0.03	0.32
ρ_p ($\mathrm{g\,cm^{-3}}$)	$0.19^{+0.10}_{-0.06}$	0.11 ± 0.02	$0.28^{+0.09}_{-0.07}$
$\log g_p$ (cgs)	2.77 ± 0.14	2.60 ± 0.06	2.93 ± 0.09
a (AU)	$0.0509^{+0.0012}_{-0.0009}$	0.0607 ± 0.0014	0.0424 ± 0.0007
T_eq (K)	1751^{+137}_{-87}	1843 ± 60	1879 ± 88
Θ	0.027 ± 0.006	0.025 ± 0.002	0.032 ± 0.004
$\langle F \rangle$ ($10^9 \mathrm{erg\,s^{-1}\,cm^{-2}}$)	$2.12^{+0.85}_{-0.38}$	2.60 ± 0.34	$2.82^{+0.65}_{-0.44}$

[a] Quantities and definitions are as in Table 11, which gives our adopted values, determined assuming circular orbits. Here we do not list parameters that are effectively independent of the eccentricity.

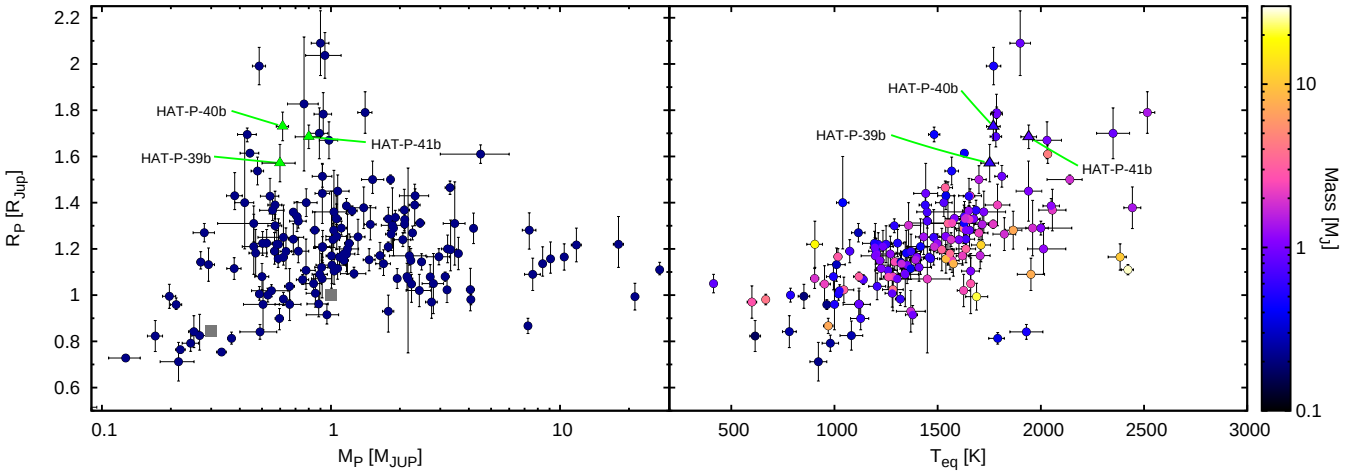

Fig. 11.— (Left): Mass–radius diagram of TEPs. HAT-P-39b through HAT-P-41b are indicated. Jupiter and Saturn are marked with filled squares. (Right): Equilibrium temperature versus radius, the mass of each planet is indicated by the color of its symbol.

N154Hr), and the NOAO Gemini/Keck time-exchange program (G329Hr). This paper presents observations made with the Nordic Optical Telescope, operated on the island of La Palma jointly by Denmark, Finland, Iceland, Norway, and Sweden, in the Spanish Observatorio del Roque de los Muchachos of the Instituto de Astrofisica de Canarias. This paper uses observations obtained with facilities of the Las Cumbres Observatory Global Telescope. The Byrne Observatory at Sedgwick (BOS) is operated by the Las Cumbres Observatory Global Telescope Network and is located at the Sedgwick Reserve, a part of the University of California Natural Reserve System. Data presented in this paper are based on observations obtained at the HAT station at the Submillimeter Array of SAO, and the HAT station at the Fred Lawrence Whipple Observatory of SAO. The authors wish to recognize and acknowledge the very significant cultural role and reverence that the summit of Mauna Kea has always had within the indigenous Hawaiian community. We are most fortunate to have the opportunity to conduct observations from this mountain.

REFERENCES

Albrecht, S., Winn, J. N., Johnson, J. A., et al. 2012, submitted to ApJ, arXiv:1206.6105
Alonso, R., et al. 2004, ApJ, 613, L153
Alsubai, K. A., Parley, N. R., Bramich, D. M., et al. 2011, MNRAS, 417, 709
Anderson, D. R., et al. 2010, ApJ, 709, 159
Anderson, D. R., Collier Cameron, A., Hellier, C., et al. 2011, A&A, 531, 60
Anderson, D. R., Collier Cameron, A., Gillon, M., et al. 2012, MNRAS, 422, 1988
Bakos, G. Á., Noyes, R. W., Kovács, G., Stanek, K. Z., Sasselov, D. D., & Domsa, I. 2004, PASP, 116, 266
Bakos, G. Á., Pál, A., Latham, D. W., et al. 2006, ApJ, 641, L57
Bakos, G. Á., Noyes, R. W., Kovács, G., et al. 2007, ApJ, 656, 552
Bakos, G. Á., et al. 2010, ApJ, 710, 1724
Bakos, G. Á., Csubry, Z., Penev, K., et al. 2012, submitted to PASP, arXiv:1206.1391
Barge, P., et al. 2008, A&A, 482, L17
Batygin, K., Stevenson, D. J., & Bodenheimer, P. H. 2011, ApJ, 738, 1
Béky, B., Bakos, G. Á., Hartman, J., et al. 2011, ApJ, 734, 109
Bonifacio, P., Monai, S., & Beers, T. C. 2000, AJ, 120, 2065
Borucki, W. J., et al. 2010, ApJ, 713, L126
Buchhave, L. A., Bakos, G. Á., Hartman, J. D., et al. 2010, ApJ, 720, 1118
Butler, R. P. et al. 1996, PASP, 108, 500
Cardelli, J. A., Clayton, G. C., & Mathis, J. S. 1989, ApJ, 345, 245
Carpenter, J. M. 2001, AJ, 121, 2851
Charbonneau, D., et al. 2009, Nature, 462, 891
Claret, A. 2004, A&A, 428, 1001
Collier Cameron, A., et al. 2007, MNRAS, 375, 951
Djupvik, A. A., & Andersen, J. 2010, in "Highlights of Spanish Astrophysics V" eds. J. M. Diego, L. J. Goicoechea, J. I. González-Serrano, & J. Gorgas (Springer: Berlin), p. 211
Droege, T. F., Richmond, M. W., & Sallman, M. 2006, PASP, 118, 1666
Eastman, J., Gaudi, B. S., & Agol, E. 2012, submitted to PASP, arXiv:1206.5798
Enoch, B., Anderson, D. R., Barros, S. C. C., et al. 2011, AJ, 142, 86
Enoch, B., Collier Cameron, A., & Horne, K. 2012, A&A, 540, 99
Fabrycky, D., & Tremaine, S. 2007, ApJ, 669, 1298
Fortney, J. J., Demory, B.-O., Désert, J.-M., et al. 2011, ApJS, 197, 9
Fűrész, G. 2008, Ph.D. thesis, University of Szeged, Hungary
Guillot, T. 2005, Annual Review of Earth and Planetary Sciences, 33, 493
Hansen, B. M. S., & Barman, T. 2007, ApJ, 671, 861
Hartman, J. D., Bakos, G. Á., Torres, G., et al. 2011, ApJ, 742, 59
Hebb, L., et al. 2009, ApJ, 693, 1920
Isaacson, H., & Fischer, D. 2010, ApJ, 725, 875
Kovács, G., Zucker, S., & Mazeh, T. 2002, A&A, 391, 369
Latham, D. W. 1992, in IAU Coll. 135, Complementary Approaches to Double and Multiple Star Research, ASP Conf. Ser. 32, eds. H. A. McAlister & W. I. Hartkopf (San Francisco: ASP), 110
Latham, D. W., et al. 2009, ApJ, 704, 1107
Latham, D. W., Borucki, W. J., Koch, D. G., et al. 2010, ApJ, 713, L140
Laughlin, G., Crismani, M., & Adams, F. C. 2011, ApJ, 729, L7
Lucy, L. B., & Sweeney, M. A. 1971, AJ, 76, 544
Mandushev, G., et al. 2007, ApJ, 667, L195
McCullough, P. R., et al. 2006, ApJ, 648, 1228
McLaughlin, D. B. 1924, ApJ, 60, 22
Noyes, R. W., Hartmann, L. W., Baliunas, S. L., Duncan, D. K., & Vaughan, A. H. 1984, ApJ, 279, 763
Pollacco, D. L., Skillen, I., Collier Cameron, A., et al. 2006, PASP, 118, 1407
Press, W. H., Teukolsky, S. A., Vetterling, W. T., & Flannery, B. P. 1992, Numerical Recipes in C. The art of scientific computing, 2nd edition. New York: Cambridge University Press. p 623.
Queloz, D., Eggenberger, A., Mayor, M., Perrier, C., Beuzit, J. L., Naef, D., Sivan, J. P., & Udry, S. 2000, A&A, 359, L13
Quinn, S. N., Bakos, G. Á., Hartman, J. D., et al. 2012, ApJ, 745, 80
Rossiter, R. A. 1924, ApJ, 60, 15
Schlegel, D. J., Finkbeiner, D. P., & Davis, M. 1998, ApJ, 500, 525
Siverd, R. J., Beatty, T. G., Pepper, J., et al. 2012, arXiv:1206.1635
Skrutskie, M. F., et al. 2006, AJ, 131, 1163
Snellen, I. A. G., et al. 2009, A&A, 497, 545
Smalley, B., Anderson, D. R., Collier Cameron, A., et al. 2012, arXiv:1206.1177
Stetson, P. B. 1987, PASP, 99, 191
Stetson, P. B. 1992, JRASC, 86, 71
Torres, G., Neuhäuser, R., & Guenther, E. W. 2002, AJ, 123, 1701
Torres, G., Konacki, M., Sasselov, D. D., & Jha, S. 2004, ApJ, 614, 979
Torres, G. et al. 2007, ApJ, 666, 121
Triaud, A. H. M. J., Collier Cameron, A., Queloz, D., et al. 2010, A&A, 524, 25
Udalski, A., Paczynski, B., Zebrun, K., et al. 2002, AcA, 52, 1
Valenti, J. A., & Fischer, D. A. 2005, ApJS, 159, 141
Valenti, J. A., & Piskunov, N. 1996, A&AS, 118, 595
Vogt, S. S. et al. 1994, Proc. SPIE, 2198, 362
Winn, J. N., Fabrycky, D., Albrecht, S., & Johnson, J. A. 2010, ApJ, 718, L145
Yi, S. K. et al. 2001, ApJS, 136, 417